

Article

# Synthesis and Structural Characterization of an Amorphous and Photoluminescent Mixed Eu/Zr Coordination Compound, a Potential Marker for Gunshot Residues

Ayla Roberta Borges Serra <sup>1</sup>, Thiago Rui Casagrande <sup>2</sup>, Juliana Fonseca de Lima <sup>3</sup>,  
 Marcelo Firmino de Oliveira <sup>2</sup>, Severino Alves Júnior <sup>1</sup>, Marcos de Oliveira Junior <sup>4,\*</sup>  
 and Osvaldo Antonio Serra <sup>2,\*</sup>

- <sup>1</sup> Fundamental Department of Chemistry, Federal University of Pernambuco, Recife 50670-901, PE, Brazil  
<sup>2</sup> Chemistry Department, Faculty of Philosophy, Sciences and Letters at Ribeirão Preto, University of São Paulo, Ribeirão Preto 14040-901, SP, Brazil  
<sup>3</sup> Institute of Chemistry, Rio de Janeiro State University, Rio de Janeiro 20550-900, RJ, Brazil  
<sup>4</sup> São Carlos Institute of Physics, University of São Paulo, P.O. Box 369, São Carlos 13566-590, SP, Brazil  
 \* Correspondence: mjunior@ifsc.usp.br (M.d.O.J.); osaserra@usp.br (O.A.S.)

**Abstract:** Hydrogels based on mixed zirconium/europium ions and benzene tricarboxylic acid were synthesized by hydrothermal reaction. A solid glass-like material is formed upon drying, showing strong reddish luminescence. The system was characterized by solid-state nuclear magnetic resonance, thermal analyses, and infrared spectroscopy. The results reveal the amorphous character of the structure and the presence of at least four types of binding modes between the metal oxide clusters and benzene tricarboxylic acid. On the other hand, thermogravimetric analysis (TGA) showed high thermal stability, with the material decomposing at temperatures higher than 500 °C. The combination of intense Eu<sup>3+</sup> luminescence with large thermal stability makes this material a strong candidate for application as a luminescent red marker for gunshot residue (GSR). As proof of concept, we show the feasibility of this application by performing shooting tests using our compound as a GSR marker. After the shots, the residual luminescent particles could be visualized in the triggered cartridge, inner the muzzle of the firearm, and a lower amount on the hands of the shooter, using a UV lamp ( $\lambda = 254$  nm). Remarkably, our results also show that the Eu<sup>3+</sup> emission for the GSR is very similar to that observed for the original solid material. These characteristics are of huge importance since they provide a chance to use smaller amounts of the marker in the ammunition, lowering the costs of potential industrial manufacturing processes.

**Keywords:** mixed-metal coordination compound; photoluminescence; solid state NMR; gun-shot-residue marker



**Citation:** Serra, A.R.B.; Casagrande, T.R.; de Lima, J.F.; de Oliveira, M.F.; Júnior, S.A.; de Oliveira Junior, M.; Serra, O.A. Synthesis and Structural Characterization of an Amorphous and Photoluminescent Mixed Eu/Zr Coordination Compound, a Potential Marker for Gunshot Residues. *Sci* **2022**, *4*, 43. <https://doi.org/10.3390/sci4040043>

Academic Editors: Claus Jacob and Ahmad Yaman Abdin

Received: 27 July 2022

Accepted: 9 November 2022

Published: 11 November 2022

**Publisher's Note:** MDPI stays neutral with regard to jurisdictional claims in published maps and institutional affiliations.



**Copyright:** © 2022 by the authors. Licensee MDPI, Basel, Switzerland. This article is an open access article distributed under the terms and conditions of the Creative Commons Attribution (CC BY) license (<https://creativecommons.org/licenses/by/4.0/>).

## 1. Introduction

Gunshot residue (GSR) is a verification of substantial significance in firearm-related crimes. Materials incorporating lanthanoids may be potential photoluminescent markers considering their unique spectroscopic properties. Lanthanoid materials can be used in several applications, from lasers [1,2] to catalysis [3–5].

Although the excited state lifetimes of Ln<sup>3+</sup> complexes are usually long, the f-f transitions are forbidden, yielding weak luminescence due to low molar absorptivity [6]. To overcome this issue, the commonly accepted method in luminescent lanthanoid compounds is called the antenna effect, which consists in sensitizing Ln<sup>3+</sup> emission by the addition of a powerfully absorbing molecule. This process can be elucidation in three steps: (1) light absorption by chromophore molecule reaching an excited state; (2) energy transfer to Ln<sup>3+</sup> ions, populating the metal ion excited state and (3) Ln<sup>3+</sup> ion light emission [7]. Among many applications, we highlight the potential of these compounds as photoluminescent

markers. More specifically, luminescent coordination compounds with high thermal stability have great potential for application as luminescent markers for Gunshot Residue (GSR) [8,9]. The luminescent markers make the GSR particles easily visible, allowing the visualization in loco, employing only a portable UV lamp. This aspect makes possible a more effective crime scene investigation, the collection of luminescent GSR (LGSR), and finally, laboratory study. According to previous works [10,11], the coordination compound, to act as a good marker, must present high photoluminescence and high thermal stability. The first is important to detect LGSR easily, and the second is to avoid decomposition during the firing.

The energy transfer process from the triplet state of organic linkers (T1) to  $\text{Ln}^{3+}$  ions depends on multiple mechanisms. We highlight that the luminescence efficiency is sensitive to the energy gap ( $\Delta E$ ) between the T1 state of the organic linker and the resonance level of the  $\text{Eu}^{3+}$  ion. Luminescence occurs only when the energy levels of the organic linker are higher than the resonance level of the  $\text{Eu}^{3+}$  ion [12]. Tricarboxylate ligands act as good sensitizers for  $\text{Eu}^{3+}$  ions, considering they have shown appropriate triplet states with an energy gap of around  $25,000 \text{ cm}^{-1}$  [8]. In this sense, we have chosen a tricarboxylate anion from benzenetricarboxylic acid ( $\text{H}_3\text{btc}$ ) as a ligand [13].

Considering the difference from the previous work [8–11], herein, we propose the synthesis of a mixed Eu-Zr coordination compound because Zr-organometallic compounds have extraordinary thermal and chemical stability. It is explained due the interaction of Zr(IV) and carboxylate oxygen atoms as they act as hard acid and base, respectively.

The compound with amorphous structure and composition is defined by TGA analysis and EDS mapping as  $[(\text{Eu}_2\text{Zr})(\text{btc})_3(\text{Hbtc})_{0.5}\cdot 6\text{H}_2\text{O}]$ , where btc and Hbtc are 1,3,5-benzenetricarboxylates, was obtained from hydrothermal synthesis. Due to the amorphous character (Figure S1), the sample was characterized by techniques sensitive to local range ordering, such as Fourier-Transformed Infra-Red (FTIR) and solid-state Nuclear Magnetic Resonance (NMR) spectroscopy. The combination of FTIR with  $^{13}\text{C}$  and  $^1\text{H}$  NMR provides a powerful approach for the identification of structural units and the determination of binding modes between the organic linkers and the metallic center [14–16].

Herein, we have also made a careful spectroscopic study applying LUMPAC software, version 1.4.1 [17], and important optical spectroscopic parameters were determined to demonstrate the applicability of the Eu/Zr coordination compound as LGSRs [17].

## 2. Materials and Methods

### 2.1. Synthesis of the $[(\text{Eu}_2\text{Zr})(\text{btc})_3(\text{Hbtc})_{0.5}\cdot 6\text{H}_2\text{O}]$

All chemicals were of AR grade, and the  $\text{Eu}_2\text{O}_3$  (Sigma-Aldrich, purity > 99.99%) was calcined before use. The synthesis route is schematically represented in Figure 1a. Benzenetricarboxylic acid (1.00 mmol) was dissolved in water/ethanol (8/8 mL) in a Teflon-lined stainless-steel reactor. Then, the aqueous  $\text{EuCl}_3$  (6 mL,  $0.100 \text{ mol}\cdot\text{L}^{-1}$ , 0.60 mmol) and  $\text{ZrCl}_4$  (0.400 mol, 0.0932 g) solutions were added to the reaction mixture. The reactor was sealed and kept at  $120 \text{ }^\circ\text{C}$  for 24 h. The reactor was then allowed to cool down at ambient conditions, reaching room temperature after 6 h. A gel compound was isolated. Subsequently, the translucent precipitate was collected by centrifugation (10,000 rpm, 10 min) and washed with  $\text{H}_2\text{O}/\text{EtOH}$  (20 mL) three times. The material was dried for 24 h at  $80 \text{ }^\circ\text{C}$  under vacuum and, after that, for another 24 h at  $150 \text{ }^\circ\text{C}$ . The final material is a solid powder with a glass-like aspect, Figure 1b. Yield: 65%. Anal. Calc. for  $[(\text{Eu}_2\text{Zr})(\text{btc})_3(\text{Hbtc})_{0.5}\cdot 6\text{H}_2\text{O}]$ : %C: 30.8, %H: 1.90 Found: %C:30.75, %H: 1.86.

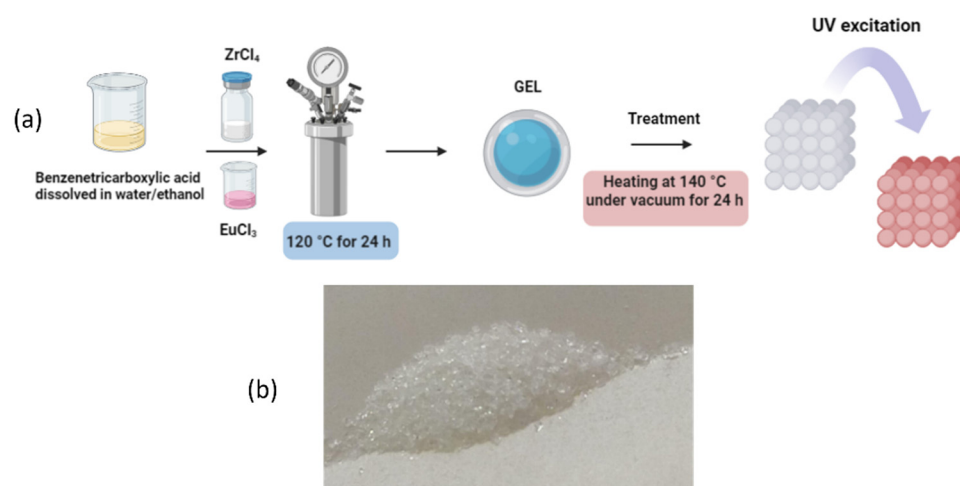


**Figure 1.** (a) Schematic illustration of the synthesis procedure; (b) The digital images of the amorphous  $[(\text{Eu}_2\text{Zr})(\text{btc})_3(\text{Hbtc})_{0.5}\cdot 6\text{H}_2\text{O}]$  coordination compound.

## 2.2. Physical Characterization

The Fourier-transformed infrared (FTIR) spectra were recorded on a Shimadzu IRprestige-21 spectrophotometer in the range  $4000\text{--}400\text{ cm}^{-1}$ . Before the measurements, the samples were dispersed in KBr pellets. Photoluminescence excitation and the emission spectra were measured on a HORIBA SPEX Fluorolog 3 fluorimeter at room temperature. Thermogravimetric analyses were carried out on a TA instruments Q-600 thermal analyzer under airflow, using a heating rate of  $10\text{ }^\circ\text{C}/\text{min}$  in the range from  $25\text{ }^\circ\text{C}$  to  $1000\text{ }^\circ\text{C}$ . Composition and morphology were examined by scanning (FEG-SEM) (Mira 3, Tescan, Czech Republic) microscope. The elemental analyses for C and H were performed using a Fisons—EA1108 CHN analyzer.

## 2.3. Solid State Nuclear Magnetic Resonance (NMR)

$^{13}\text{C}$  and  $^1\text{H}$  solid-state NMR spectra were measured on a Bruker Avance Neo spectrometer operating at 14.1 T (600 MHz for  $^1\text{H}$  Larmor frequency) equipped with a Bruker HX 1.3 mm probe. Before the NMR measurements, the samples were ground and dried at  $160\text{ }^\circ\text{C}$  for 20 h in an ambient atmosphere.  $^1\text{H}$  MAS spectra were obtained with the EASY (Elimination of Artifacts in NMR Spectroscopy) pulse sequence [18], which eliminates fast relaxing probe background signal. The spinning speed for MAS was 60 kHz, and the  $\pi/2$  pulse length of 1.0  $\mu\text{s}$ . The recycle delays for the first and second blocks in the sequence were set to 2 s and 0.5 ms, and 32 scans were acquired.  $^{13}\text{C}\{^1\text{H}\}$  cross-polarization magic angle spinning (CPMAS) spectra were recorded at a 30 kHz spinning rate using contact times ranging from 50  $\mu\text{s}$  to 1.0 ms and recycle delay of 2 s. Direct polarization  $^{13}\text{C}$  spectra were recorded using the DEPTH pulse sequence to suppress probe background signal [19], with  $\pi/2$  pulse duration of 2.75  $\mu\text{s}$ , recycle delay of 60 s and MAS at 30 kHz. All  $^{13}\text{C}$ -observed spectra were acquired with  $15^\circ/-15^\circ$  TPPM [20] proton decoupling in the  $^1\text{H}$  channel during the data acquisition.  $^1\text{H}\text{--}^{13}\text{C}\text{--}^1\text{H}$  double cross-polarization (double-CP) experiments were performed at 60 kHz MAS, using the pulse sequence described by Baccile et al. [21], where polarization is first transferred from  $^1\text{H}$  to  $^{13}\text{C}$  spin followed by a block where  $^{13}\text{C}$  magnetization is stored on the z-axis while  $^1\text{H}$  magnetization is saturated by a train of ten (10)  $\pi/2$  pulses [21]. Finally,  $^{13}\text{C}$  magnetization is converted back to xy-plane and polarization is transferred from  $^{13}\text{C}$  to nearby  $^1\text{H}$  and detected on the  $^1\text{H}$  channel. The first contact pulse was fixed at 2 ms, while the second pulse was fixed at 500  $\mu\text{s}$  to selectively excite the  $^1\text{H}$  species in the local environment of  $^{13}\text{C}$  species. Typical  $\pi/2$  pulse lengths were adjusted to 1.15 and 2  $\mu\text{s}$  for  $^1\text{H}$  and  $^{13}\text{C}$ , respectively and up to 8192 scans were accumulated. Adiabatic tangentially ramped contact pulses [22] on the  $^1\text{H}$  channel ( $\nu_{\text{rf}} = 80 \pm 20\text{ kHz}$ ) and squared pulses on the X channel ( $\nu_{\text{rf}} = 140\text{ kHz}$ ) were used to achieve  $^1\text{H} \rightarrow ^{13}\text{C}$  and  $^{13}\text{C} \rightarrow ^1\text{H}$  polarization transfer. No  $^{13}\text{C}$  decoupling was em-

ployed during the  $^1\text{H}$  acquisition. Indirectly detected 2D  $^1\text{H}$ - $^{13}\text{C}$  heteronuclear correlation (HETCOR) spectra were acquired with a modification of the double-CP sequence described above. After the first polarization transfer, the  $^{13}\text{C}$  coherences are allowed to evolve during time  $t_1$ , while  $^1\text{H}$  decoupling was achieved by a single  $2\ \mu\text{s}$   $\pi$  pulse applied in the middle of the  $t_1$  period, as described by Wiench et al. [23]. The first CP block was set to 1 ms in order to maximize  $^1\text{H}$ - $^{13}\text{C}$  polarization transfer, and the second CP was set to  $500\ \mu\text{s}$ . 2D  $^1\text{H}$ - $^1\text{H}$  double-quantum—single-quantum (DQ-SQ) correlation NMR experiments were performed at 60.8 kHz MAS, using  $R14_4^5$  symmetry-based homonuclear recoupling scheme and no homonuclear decoupling during DQ evolution [24]. Excitation and reconversion times were  $65.8\ \mu\text{s}$  (four rotor cycles), and the increment interval in the indirect dimension was set to  $16.4\ \mu\text{s}$  (rotor period); 256  $t_1$  increments were acquired, with 16 scans of accumulations for each  $t_1$  increment and 2 s recycle delay.  $^{13}\text{C}$  and  $^1\text{H}$  chemical shifts are reported relative to tetramethylsilane (TMS) using  $\alpha$ -glycine as a secondary reference,  $^{13}\text{C}$ - $\delta_{(\text{C}=\text{O})} = 176.5\ \text{ppm}$  and  $^1\text{H}$ - $\delta_{(\text{NH}_3)} = 8.5\ \text{ppm}$  [25,26].

#### 2.4. Gunshot Residue (GSR)

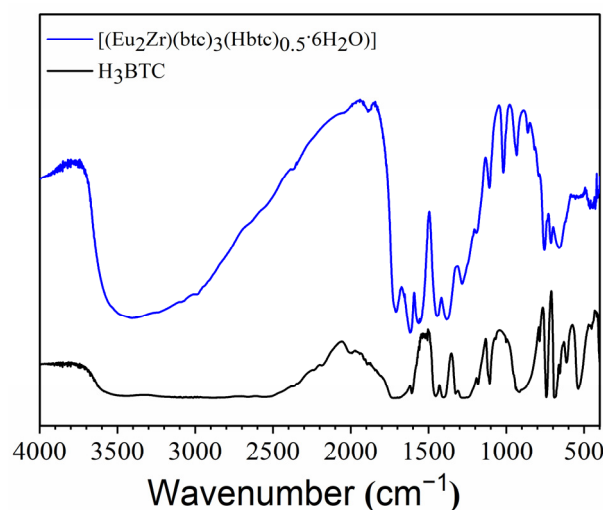
GSR tests were conducted following similar conditions reported by Marques, L. F. et al. (2020). Eu/Zr coordination compounds were added to the gunpowder in a percentage of 5 and 10% (15 and 30 mg). A 0.380 pistol (Taurus, 638 Pro) equipped with cartridges (EXPO Gold Hex GR) containing the modified gunpowder was employed. The shots were fired against a wood target, and the shooter's position was fixed 2 m from the target. Gunshot residues that remained inside the firearm and cartridges and those scattered on the floor were detected by UV light (254 nm). Images were collected by a cellphone camera (Apple iPhone 12, camera 12MP).

### 3. Results

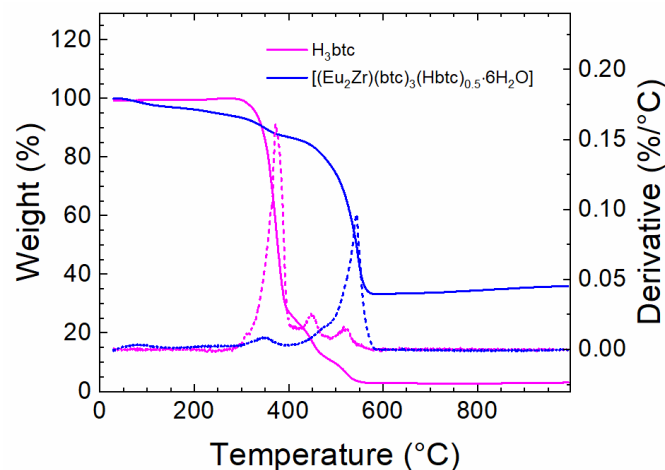
#### 3.1. Vibrational Spectroscopy (Infrared) and Thermal Analysis

Figure 2 displays the infrared spectra of the synthesized  $[(\text{Eu}_2\text{Zr})(\text{btc})_3(\text{Hbtc})_{0.5}\cdot 6\text{H}_2\text{O}]$  material and pure ligand  $\text{H}_3\text{btc}$ . Typically, the absorption bands of  $1613$ – $1560\ \text{cm}^{-1}$  and  $1453/1399\ \text{cm}^{-1}$  were correlated to asymmetric and symmetric stretching vibrations of  $\text{COO}^-$ , respectively. The difference between symmetric and asymmetric vibration frequencies is larger than  $160\ \text{cm}^{-1}$ , which does not let us rule out the existence of both monodentate and bidentate carboxylate species [13,27]. These observations indicate the coordination of lanthanoid ions by carboxylate groups from the ligand. The bands at  $1111$  and  $935\ \text{cm}^{-1}$  were assigned to the in-plane bending  $\delta(\text{CCH})$  and out-of-plane bending  $\gamma(\text{CCH})$  of the aromatic ring in the btc linker. The three peaks between  $650$ – $780\ \text{cm}^{-1}$  were compatible with the C-H out-of-plane of the benzene ring. The wide band around  $1750$ – $3000\ \text{cm}^{-1}$  is related to the stretching modes of the hydroxyl species of the  $\text{COOH}$  group and aromatic-CH in the structure of  $\text{H}_3\text{btc}$ . The band localized at  $1713\ \text{cm}^{-1}$  suggests that the  $\text{H}_3\text{btc}$  ligand was not completely deprotonated, as also confirmed by the NMR results described below.

Figure 3 exhibits the TGA curves of  $[(\text{Eu}_2\text{Zr})(\text{btc})_3(\text{Hbtc})_{0.5}\cdot 6\text{H}_2\text{O}]$  after dehydration at  $160\ ^\circ\text{C}$  for 24h in comparison with the curve for the  $\text{H}_3\text{btc}$  precursor. A weight loss of 10% between  $25$  and  $200\ ^\circ\text{C}$  indicated the presence of water molecules (found at 9%, calculated at 8.8%). The main loss occurs between  $450$ – $597\ ^\circ\text{C}$ , with a maximum at  $547\ ^\circ\text{C}$ , which is much higher than the decomposition temperature of the  $\text{H}_3\text{btc}$  precursor ( $373\ ^\circ\text{C}$ ), indicating the higher thermal stability of this new compound (see Figure 3). The observed residue, at  $1000\ ^\circ\text{C}$ , agrees with a possible compound described as  $[(\text{Eu}_2\text{Zr})(\text{btc})_3(\text{Hbtc})_{0.5}\cdot 6\text{H}_2\text{O}]$  (found 38.0%, calculated 39%). We consider the residue to be  $\text{Eu}_2\text{O}_3 + \text{ZrO}_2$ . The EDS analysis (Figure S2) confirmed the expected compound formula proposed by TGA.



**Figure 2.** Infrared Spectra for  $[(\text{Eu}_2\text{Zr})(\text{btc})_3(\text{Hbtc})_{0.5}\cdot 6\text{H}_2\text{O}]$  compound and for the benzenetricarboxylic acid ( $\text{H}_3\text{btc}$ ) precursor.



**Figure 3.** TGA curves (solid lines) for  $[(\text{Eu}_2\text{Zr})(\text{btc})_3(\text{Hbtc})_{0.5}\cdot 6\text{H}_2\text{O}]$  and  $\text{H}_3\text{btc}$  represent the successive mass losses. The derivatives of the TGA curves are shown as dashed lines.

Comparing the TGA curves of the material containing the Eu/Zr mixture with the material containing only Eu (Figure S3), we observed a difference of more than  $100\text{ }^\circ\text{C}$  in the decomposition temperature. Considering that thermal stability is one of the main characteristics of the material to be applied in LSGR, the mixture of metallic ions is a good indicator for this application.

### 3.2. Solid-State NMR Characterization

Additional details about the structure can be obtained by solid-state  $^{13}\text{C}$  and  $^1\text{H}$  NMR. More specifically, in complement with FTIR results, NMR can give information about the coordination modes of the carboxylate species from the btc linker. Figure 4 shows  $^{13}\text{C}$  MAS NMR spectra for  $[(\text{Eu}_2\text{Zr})(\text{btc})_3(\text{Hbtc})_{0.5}\cdot 6\text{H}_2\text{O}]$  obtained with  $^{13}\text{C}\{^1\text{H}\}$  CP with varying contact time (50, 100, 500 and 1000  $\mu\text{s}$ ) and  $^{13}\text{C}$  direct polarization. Only the region where peaks from btc are observed is displayed. The complete  $^{13}\text{C}$  spectrum is provided as supplemental material, showing additional resonances attributed to ethanol molecules adsorbed on the sample (see Figure S4 in the Supporting Information). The schemes for the expected coordination modes of btc with the metallic cluster are also shown in Figure 4 [14–16]. Due to the amorphous character of the sample, the  $^{13}\text{C}$  NMR lines are poorly resolved. Deconvolution of the spectra into Gaussian lines was performed by

observing the lineshape variations as a function of the contact time in the CP experiment. The best-fit deconvolutions are displayed in Figure 4, and the parameters for the direct polarization experiment are given in Table 1. The position and line widths for each Gaussian component were fixed among the various spectra. The deconvolutions show lines centered at 132, 135, 164, 167, 171, 174 and 185 ppm. The lines centered at 129, and 133 ppm are, respectively, attributed to the aromatic carbons C2 and to the quaternary carbons C1 in btc (see Scheme in Figure 4). These attributions are supported by the relative intensity variations of both components as a function of the CP contact time. The protonated species, C2, shows relatively high intensities for low contact times, while the non-protonated C1 species needs more time for magnetization build-up. The line at 185 ppm may be attributed to carboxylate groups with chelating coordination with the metallic center (V in the scheme of Figure 4), as a downfield shift of 5 to 13 ppm is expected for these species when compared to bidentate or monodentate bridging ones [14–16]. The line at 164 ppm corresponds to non-coordinated (I), while the line at 167 ppm corresponds to bidentate bridged carboxylate groups performing H-bonds with MOH species (IV), as confirmed by the double resonance experiments described below. According to FTIR results, the presence of monodentate coordination cannot be discarded. From our results, we could not distinguish between monodentate (II) and bidentate species (III), being the attribution of the lines around 171 and 174 ppm is still not resolved [15].

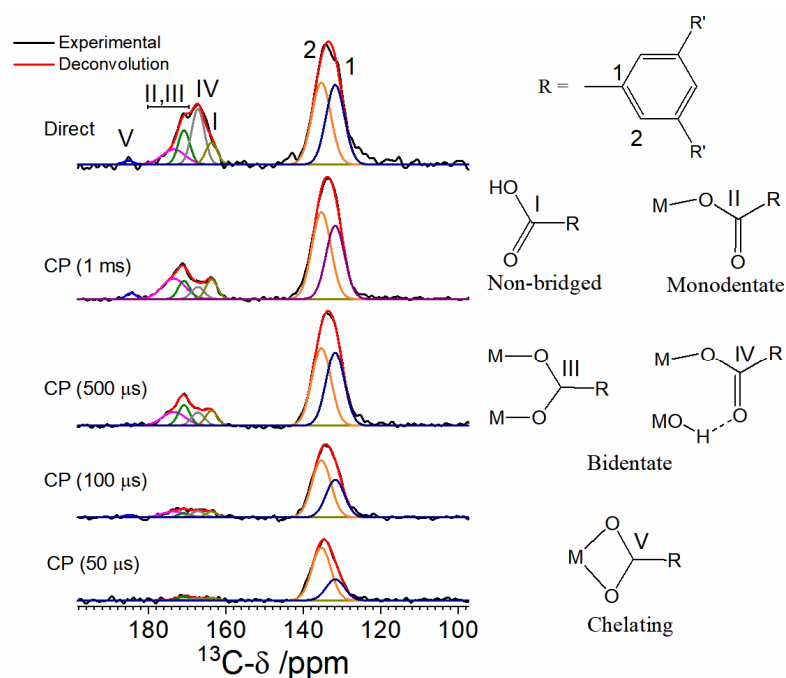


**Figure 4.** (Left):  $^{13}\text{C}$  MAS NMR spectra (black curves) obtained by  $^{13}\text{C}\{^1\text{H}\}$  cross-polarization (CP) and direct polarization on  $^{13}\text{C}$  with background suppression and  $^1\text{H}$  decoupling (Direct). Colored curves are spectral deconvolutions into Gaussian functions. Assignments for the observed peaks are given as roman numerals, corresponding to the scheme on the right. Assignments for species II and III could not be unequivocally provided, both lies in the region indicated by an horizontal line in the figure. (Right): Possible coordination modes for the carboxylate groups in btc with the metallic species. R' is a carboxylate group in one of the coordination modes I to V.

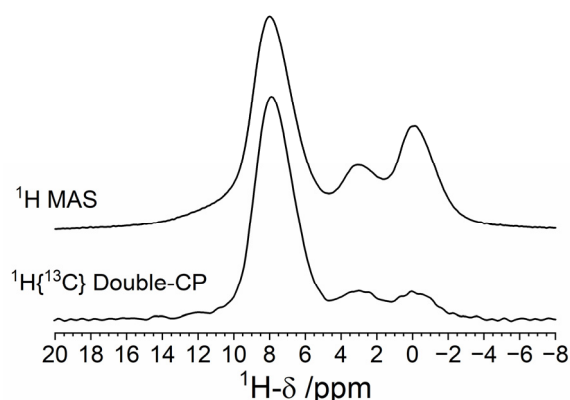
**Table 1.** Spectral parameters were obtained from the deconvolution of the  $^{13}\text{C}$  NMR spectrum measured with direct polarization.  $\delta_{\text{iso}}$  is the isotropic chemical shift, FWHM is the full-width at half-maximum, and I is the relative area for each spectral component.

Attribution	$\delta_{\text{iso}}$ ( $\pm 1$ ppm)	FWHM ( $\pm 0.5$ ppm)	I ( $\pm 2\%$ )
C1	132	5.6	31
C2	135	5.8	33
I	164	3.6	5
II, III <sup>a</sup>	167/171	3.9/3.6	15/8
IV	174	7.1	7
V	185	3.1	1

<sup>a</sup> Attributions to species II and III could not be unequivocally given.

Finally, the  $^{13}\text{C}$  spectrum obtained by direct polarization (Figure 4, top) provides quantitative information. The parameters for this spectrum are displayed in Table 1. An intensity ratio of approximately 1:1:1 is observed for the three types of C in btc, validating the quantitative character of the experiment. A considerable fraction of carboxylate groups is in the non-coordinated configuration, about 14%, corresponding to an average of 0.4 non-coordinated COOH groups for each btc molecule. These species can be understood as structural defects, and their relatively high concentration is in agreement with the amorphous character of the sample and the absence of pores (as observed in nitrogen adsorption experiments, not shown).

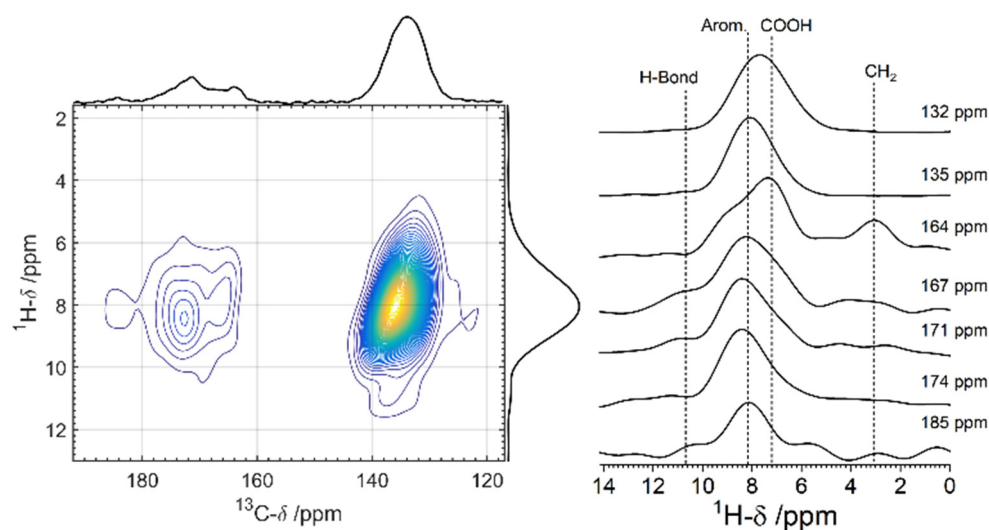
Figure 5 shows the solid state  $^1\text{H}$  spectrum (top) measured under 60 kHz MAS. Even at high rotation speeds, the  $^1\text{H}$  spectrum still presents a complex structure, due to the presence of many H species, besides those from btc, such as molecules or agglomerates of water adsorbed on the material. To simplify the  $^1\text{H}$  spectrum, a  $^1\text{H}\{^{13}\text{C}\}$  Double-CP experiment was also performed (Figure 5, bottom spectrum) [22]. In this experiment, only those  $^1\text{H}$  dipolarly coupled to  $^{13}\text{C}$  are observed. This spectrum shows  $^1\text{H}$  lines at three chemical shift regions: 8.3 ppm, corresponding to unresolved  $^1\text{H}$  signals from the aromatic ring and OH in free carboxylate groups, and 3.4, 0.3 ppm, corresponding respectively to  $\text{CH}_2$  and  $\text{CH}_3$  in ethanol molecules adsorbed on the structure [28]. By comparing both spectra in Figure 5, the  $^1\text{H}$  NMR signal for proton species not coupled to  $^{13}\text{C}$  can be identified. A broad shoulder around 10 ppm is observed for the  $^1\text{H}$  MAS spectrum, which is not present for the  $^1\text{H}\{^{13}\text{C}\}$  Double-CP one. This resonance can be attributed to OH species or water molecules H-bonded to the metal oxide [14].



**Figure 5.**  $^1\text{H}$  MAS (top) and  $^1\text{H}\{^{13}\text{C}\}$  Double-CP (bottom) spectra for the  $[(\text{Eu}_5\text{Zr}_3)(\text{btc})_9(\text{H}_2\text{O})_{18}]$  compound. Both spectra were obtained under a 60 kHz MAS spinning rate.

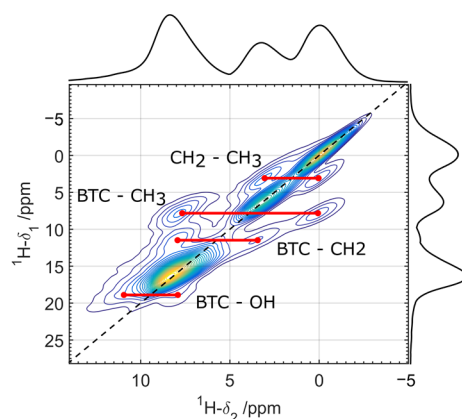
In order to confirm the  $^{13}\text{C}$  attributions for the different coordination modes of btc, a  $^1\text{H}\{^{13}\text{C}\}$  Double-CP HETCOR experiment was performed. The 2D spectrum is displayed in Figure 6. Relatively long CP contact times (500  $\mu\text{s}$ ) were used in the experiment in order to observe correlations for the non-protonated carbon species (C1 and I to V in the scheme of

Figure 4). This figure also displays the  $^1\text{H}$  dimension projections corresponding to the  $^{13}\text{C}$  shifts at 185, 174, 171, 167, 164, 135 and 130 ppm (obtained from the integration over a range of  $\pm 2$  ppm). The protons bound to the C2 carbon of the btc present a resonance centered at 8.1 ppm, as shown by the  $^1\text{H}$  projection for this site. As shown by the projections, the main source of polarization for carbon species resonating at 167 to 185 ppm comes from the aromatic protons, indicating that these species correspond to carboxylate groups coordinated with the metallic oxide species. From the  $^{13}\text{C}$  chemical shift, the line at 185 ppm is attributed to the chelating coordination of the btc with on metallic atom (V, see scheme in Figure 4) [13–15]. The  $^1\text{H}$  projection for the  $^{13}\text{C}$  species resonating at 167 ppm shows a shoulder at around 10.7 ppm, which may be attributed to OH species from the metallic cluster, letting us attribute the  $^{13}\text{C}$  line at 167 ppm to bidentate bridged btc sharing one proton with the metallic species via H-bond. As discussed before, unfortunately, the lines at 174 and 171 ppm cannot be unequivocally attributed [15]. Both lines correspond to bidentate (III) and monodentate (II) bridging modes. The existence of both modes is supported by FTIR results.  $^{13}\text{C}$  resonating at 164 ppm, on the other hand, correlates with protons resonating at 7.3 ppm. This chemical shift can be associated with COOH groups from non-coordinated carboxylate species in btc. A correlation peak with  $^1\text{H}$  shift at 3.5 ppm, attributed to  $\text{CH}_2$  groups from ethanol, is also observed for this species, indicating special proximity between COOH groups in btc and ethanol. Finally, the  $^1\text{H}$  projection for carbon C2 presents a broad line centered at 7.6 ppm, which can be attributed to the mutual interaction with  $^1\text{H}$  in C3 and COOH.



**Figure 6.** Two-dimensional  $^1\text{H}\{^{13}\text{C}\}$  Double-CP HETCOR [(Eu<sub>2</sub>Zr)(btc)<sub>3</sub>(Hbtc)<sub>0.5</sub>·6H<sub>2</sub>O)] (left) and traces taken from the vertical dimension, showing partial  $^1\text{H}$  spectra (normalized by intensity) corresponding to several shifts of  $^{13}\text{C}$  (right). The experiment was carried out under MAS conditions at 60 kHz with  $^1\text{H}$  detection. The numbers indicated in the two-dimensional spectrum correspond to the carbon labeling in Figure 4.

Figure 7 shows the 2D DQ-SQ  $^1\text{H}$ - $^1\text{H}$  correlation spectrum for [(Eu<sub>2</sub>Zr)(btc)<sub>3</sub>(Hbtc)<sub>0.5</sub>·6H<sub>2</sub>O)]. The spectrum reveals dipolar coupling between  $^1\text{H}$  in  $\text{CH}_2$  and  $\text{CH}_3$  groups in ethanol and between btc protons with  $\text{CH}_3$ ,  $\text{CH}_2$  and OH groups from the metal oxide cluster, revealing spatial proximity between these groups. Most probably, ethanol OH groups coordinate with btc  $\text{COO}^-$  ones by hydrogen bond. The same conclusions are drawn from  $^1\text{H}$ - $^1\text{H}$  exchange spectroscopy (see Figure S5 in the Supporting Information). The interaction of ethanol with btc species prevents the coordination with the metallic species, blocking the growth of the structure. Finally, the presence of self-correlation peaks on the diagonal of the DQ-SQ indicates intermolecular proximity between btc moieties, which is an indication of a collapsed poreless structure.



**Figure 7.** 2D  $^1\text{H}$  DQ-SQ correlation spectrum for  $[(\text{Eu}_2\text{Zr})(\text{btc})_3(\text{Hbtc})_{0.5}\cdot 6\text{H}_2\text{O}]$  measured under 60 kHz MAS using  $R14_4^5$  symmetry-based homonuclear recoupling and no homonuclear decoupling during DQ evolution. The red lines indicate the presence of  $^1\text{H}$ - $^1\text{H}$  correlations.

### 3.3. Photoluminescence Studies

The photophysical properties exhibited by the compound  $[(\text{Eu}_2\text{Zr})(\text{btc})_3(\text{Hbtc})_{0.5}\cdot 6\text{H}_2\text{O}]$  has been studied. The  $^5\text{D}_0 \rightarrow ^7\text{F}_2$  transition of  $\text{Eu}^{3+}$  ion centered at 614 nm is hypersensitive and its accompaniment, at 300 K, gives the excitation spectrum depicted in Figure 8a. The spectrum exhibits intense broad-band emission between 200 and 310 nm, maximum at 280 nm, related to LCCT from ligand btc to Zr/Eu metal and the usual sharp lines determined by f-f transitions of  $\text{Eu}^{3+}$  ions. The UV-VIS spectra, Figure S6, also showed the strongest adsorption in this range, not being possible to observe the absorption bands related to  $^7\text{F}_0 \rightarrow ^7\text{L}_6$  and  $^7\text{F}_0 \rightarrow ^5\text{D}_2$  transitions.

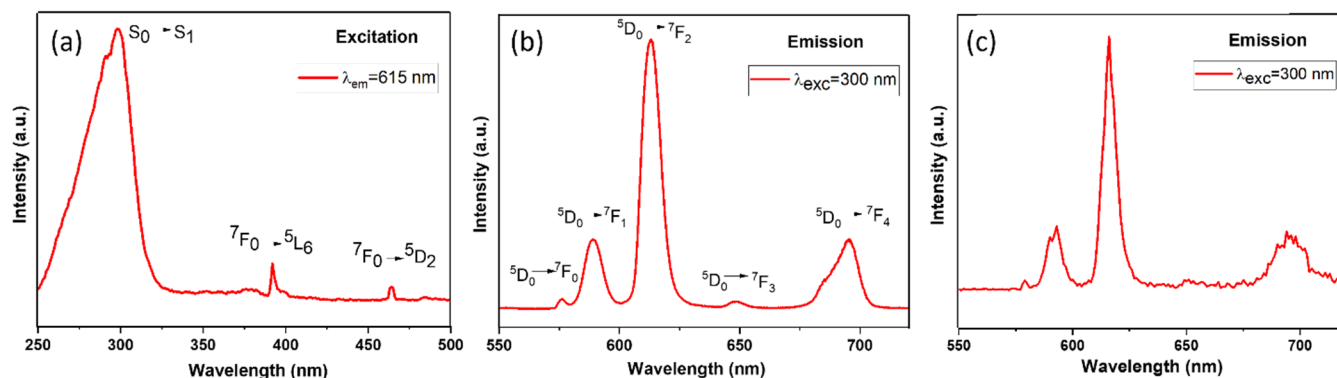


**Figure 8.** (a) Excitation ( $\lambda_{\text{em}} = 615$  nm), (b) emission ( $\lambda_{\text{exc}} = 300$  nm) spectra of  $[(\text{Eu}_2\text{Zr})(\text{btc})_3(\text{Hbtc})_{0.5}\cdot 6\text{H}_2\text{O}]$  and (c) emission ( $\lambda_{\text{exc}} = 300$  nm) spectra of  $[(\text{Eu}_2\text{Zr})(\text{btc})_3(\text{Hbtc})_{0.5}\cdot 6\text{H}_2\text{O}]$  in GSR, recorded in the solid state.

Besides the sharp excitation assigned to  $^7\text{F}_0 \rightarrow ^5\text{D}_2$  (465 nm) intra-configurational  $4f^6$  transition of  $\text{Eu}^{3+}$ , the strong broad-band excitation at 280 nm can be attributed to the ligand absorption band, which indicates that the sensitization occurs by the btc ligands (antenna effect).

The emission spectrum, Figure 8b, was obtained at 300 K, exciting the complex at 300 nm (singlet state of btc). Emission bands coming from  $^5\text{D}_0$  levels were observed in 590 nm for  $^5\text{D}_0 \rightarrow ^7\text{F}_1$ ; 613 nm for  $^5\text{D}_0 \rightarrow ^7\text{F}_2$ ; 648 nm for  $^5\text{D}_0 \rightarrow ^7\text{F}_3$ ; and 695 nm for  $^5\text{D}_0 \rightarrow ^7\text{F}_4$ . The  $^5\text{D}_0 \rightarrow ^7\text{F}_0$  has a width at half height of  $120\text{ cm}^{-1}$ , as the agreement of several slightly different conformations, as in polymeric structures [29,30]. The  $^5\text{D}_0 \rightarrow ^7\text{F}_2$  transition is mostly influenced by the dynamic coupling since the  $^7\text{F}_2$  sublevels are in the energy range of important vibrations. The  $^5\text{D}_0 \rightarrow ^7\text{F}_1$  transition is not perturbed since the  $^7\text{F}_1$  sublevels lie in an energy range in which there are no intense IR or Raman bands.

It is observed that the electric dipole prevailed compared to a magnetic dipole since the  ${}^5D_0 \rightarrow {}^7F_2$  transition shows higher values of intensity than the  ${}^5D_0 \rightarrow {}^7F_1$  transition. To determine the symmetry site of the  $\text{Eu}^{3+}$  ion, the ratio of the intensities between  ${}^5D_0 \rightarrow {}^7F_2$  and  ${}^5D_0 \rightarrow {}^7F_1$  transitions is studied [31,32]. The ratio calculated from Figure 8b is about 3.95, suggesting a low symmetry site (non-centrosymmetric environment) [31–33] for  $\text{Eu}^{3+}$  ion in  $[(\text{Eu}_2\text{Zr})(\text{btc})_3(\text{Hbtc})_{0.5}\cdot 6\text{H}_2\text{O}]$ . According to the  ${}^5D_0 \rightarrow {}^7F_0$  transition, it is possible to define the micro-symmetry, as in the  $C_{nv}$ ,  $C_n$ , or  $C_s$  point groups, since this transition is observed only for low micro-symmetry [34]. Only one peak is verified for  ${}^5D_0 \rightarrow {}^7F_0$  transition (Figure 8b), centered at 576.3 nm ( $\sim 1735.21 \text{ cm}^{-1}$ ); this observation suggests that all  $\text{Eu}^{3+}$  ions emitting sites are equivalent. The lifetime of the  ${}^5D_0$  excited state is  $\tau = 0.22 \pm 0.01 \text{ ms}$  (Figure S6), which can be due to high deactivation rates by the oscillators O-H from water or ethanol molecules coordinated with the ion. Generally, OH species can bind to the  $\text{Eu}^{3+}$  ions, as demonstrated by solid-state NMR since the ligand does not occupy the entire coordination sphere. The low luminescence quantum yields, and lifetimes can be explained by the deactivation process that occurs from the vibronic coupling between Eu and OH oscillators. The large nonradiative rates also prove this supposition.

Table 2 present the values obtained from the experimental luminescence study, such as the radiative ( $A_{\text{rad}}$ ) and nonradiative ( $A_{\text{nrad}}$ ) emission rates, intensity parameters ( $\Omega_2$  and  $\Omega_4$ ) and quantum efficiency ( $\eta$ ) for  $[(\text{Eu}_2\text{Zr})(\text{btc})_3(\text{Hbtc})_{0.5}\cdot 6\text{H}_2\text{O}]$  compound. The water molecules coordinated with  $\text{Eu}^{3+}$  ions favor the nonradiative decay due to the vibronic coupling of the O-H oscillators. Based on that, it is possibly related to the experimental radiative rate ( $A_{\text{rad}} = 354.1 \text{ s}^{-1}$ ), nonradiative rate ( $A_{\text{nrad}} = 4191.4 \text{ s}^{-1}$ ), and the short lifetime  $\tau$  of 0.22 ms with the relaxation process. Whereas the described compound showed a low  $\Omega_4$  value (see Table 2), we can assume a considerable rigidity related to the structure [34].

**Table 2.** Experimental luminescence parameters. Experimental Nonradiative ( $A_{\text{nrad}}$ ), Radiative ( $A_{\text{rad}}$ ) Decay Rates; Intensity Parameters  $\Omega_2$  and  $\Omega_4$ ; Quantum Efficiency ( $\eta$ ) and lifetime ( $\tau$ ).

$A_{\text{rad}}$	$A_{\text{nrad}}$	$\Omega_2 (10^{-20} \text{ s})$	$\Omega_4 (10^{-20} \text{ s})$	$\eta$	$\tau (\text{ms})$
354.08	4191.37	7.0	5.73	7.79	0.22

### 3.4. Experimental test of $[(\text{Eu}_2\text{Zr})(\text{btc})_3(\text{Hbtc})_{0.5}\cdot 6\text{H}_2\text{O}]$ Compound as a Red Luminescent Marker for Ammunition

The experimental results obtained for the Eu/Zr compound indicated a strong emission of light in the red region when submitted to the application of ultraviolet light ( $\lambda = 254 \text{ nm}$ ). TGA and DSC studies also indicated considerable thermal stability for this compound, which was in accordance with previous studies reported in the literature for similar Eu/Zr compounds [9]. These characteristics allowed the proposed compound to be used as an alternative chemical marker in GSR analysis. After the shots, the luminescent residue inside the cartridges of the 0.380 pistol gun was identified using a commercial 254 nm ultraviolet light lamp. It was possible to produce several shots with the marked 0.380 ammunition using 15 to 30 mg of the chemical marker. It is important to mention that the total mass of commercial gunpowder ammunition consisted of 345mg per capsule. It was possible to obtain multiple points of luminescent detection in different regions of the pistol and also in the cartridges, even when minimum amounts of 15 mg of the compound were used. In Figure 9a–f, it is clearly possible to observe the images obtained under UV light excitation of the luminescent residues, in the ejected capsule, on target and inside the gun barrel. It was also possible to analyze by luminescence the LGSR recovered from the gun (Figure 8c), where the spectra maintain similar spectra from the original one. In fact, although the spectra show more noise due to the low amount of material recovered, the spectral profile is maintained, and the intensity ratio of the  ${}^5D_0 \rightarrow {}^7F_1/{}^5D_0 \rightarrow {}^7F_2$  in both cases was near 0.261, which confirms no modification in the compound after the shot. Since the luminescent properties of the compound remained unaltered, it is indicative that this material can be effectively used as tagging material for ammunition.

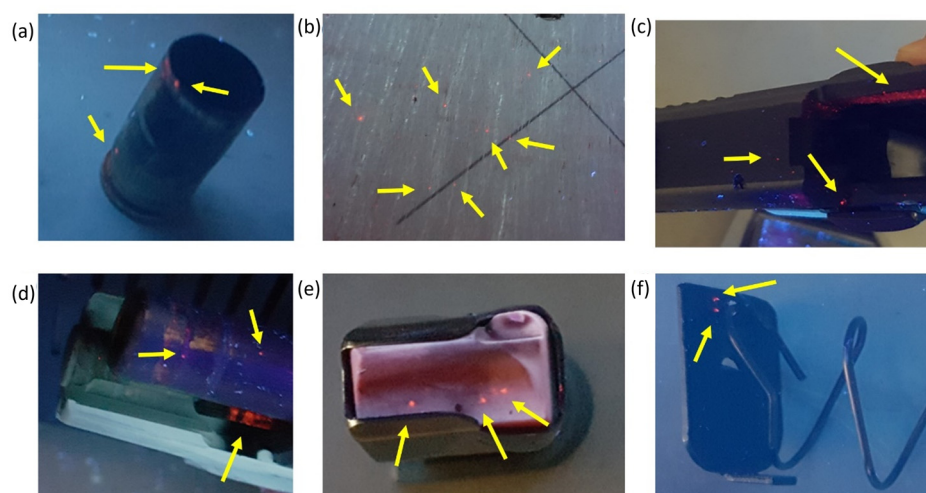


**Figure 9.** Red residual luminescent in GSR: (a) in the ejected capsule; (b) in the triggered cartridge; (c) inside the bolt of the firearm; (d) inside the slide of the firearm; (e) over the magazine and (f) under the magazine. UV light irradiation,  $\lambda = 254$  nm.

#### 4. Conclusions

The hydrothermal method was employed successfully to obtain a glass-like aspect mixed Zr/Eu coordination compound with benzene tricarboxylic acid (H<sub>3</sub>btc) as marker of gunshot residues (GSRs). Powder XRD results show that the compound has an amorphous structure. Solid-state NMR results reveal the connectivity between the btc organic linker and the Zr/Eu metal oxide clusters. The results show two binding modes, chelating, and bridging. Quantitative <sup>13</sup>C NMR results also reveal the presence of an expressive amount of non-coordinated COOH groups. On average, we estimate that there are 1.7 (out of three) non-bridging COOH per btc molecule, in total agreement with elemental analysis. This high degree of non-bridging sites explains the amorphous character of the sample and the absence of pores, contrary to the observed for other btc-based metal-organic compounds. [(Eu<sub>2</sub>Zr)(btc)<sub>3</sub>(Hbtc)<sub>0.5</sub>·6H<sub>2</sub>O)] compound structure was elucidated, and its photoluminescence study was carefully conducted. The ligand presence allowed an efficient intramolecular energy transfer resulting in an intense red emission by Eu<sup>3+</sup> ions. Thermogravimetric analysis showed the high thermal stability of our Eu/Zr compound. Considering the thermal stability and luminescence data, [(Eu<sub>2</sub>Zr)(btc)<sub>3</sub>(Hbtc)<sub>0.5</sub>·6H<sub>2</sub>O)] was added to gunpowder and gunshots were evaluated, the presence of Eu/Zr coordination compound enabled visual detection of the particles on the floor, in the firearm and cartridges. Although other lanthanoid compounds have been reported as ammunition markers, there is no photoluminescence information regarding the Eu/Zr coordination compound derived from benzene tricarboxylic acid. Mixed Eu/Zr luminescent particles with unique characteristics can support criminal investigations involving firearms.

**Supplementary Materials:** The following supporting information can be downloaded at: <https://www.mdpi.com/article/10.3390/sci4040043/s1>, Figure S1: XRD pattern of luminescent compound [(Eu<sub>2</sub>Zr)(btc)<sub>3</sub>(Hbtc)<sub>0.5</sub>·6H<sub>2</sub>O)]; Figure S2: Chemical composition (EDS) analysis of [(Eu<sub>2</sub>Zr)(btc)<sub>3</sub>(Hbtc)<sub>0.5</sub>·6H<sub>2</sub>O)]; Figure S3: TGA/DSC analysis of Eu-btc; Figure S4: <sup>13</sup>C{<sup>1</sup>H} CPMAS spectrum of the compound [(Eu<sub>2</sub>Zr)(btc)<sub>3</sub>(Hbtc)<sub>0.5</sub>·6H<sub>2</sub>O)]; Figure S5: 2D <sup>1</sup>H-<sup>1</sup>H EXSY spectra for [(Eu<sub>2</sub>Zr)(btc)<sub>3</sub>(Hbtc)<sub>0.5</sub>·6H<sub>2</sub>O)] measured at two mixing times, 1 ms and 10 ms, under 60 kHz MAS. The dashed lines indicate the presence of <sup>1</sup>H-<sup>1</sup>H correlations for the longer mixing time. For short mixing times (1 ms), the spectrum reveals no exchange between distinct <sup>1</sup>H species. For longer mixing times, cross-peaks revealing exchange between <sup>1</sup>H in CH<sub>2</sub> and CH<sub>3</sub> groups in ethanol become visible, while the same is true for the correlation between btc protons with CH<sub>2</sub> and OH groups from the metal oxide cluster, revealing spatial proximity between these groups. Most probably, ethanol OH groups coordinate with btc COO<sup>-</sup> ones by hydrogen bond. The interaction of ethanol with btc species prevents the coordination with the metallic species, blocking the growth of the structure.

Experimental details: experiments were performed at 60 kHz using a 1.4 s recycle delay and mixing times of 1 and 10 ms. A total of 512 points were collected in the indirect dimension with a time increment of 16.67  $\mu$ s, corresponding to a spectral width of 60 kHz; Figure S6: UV-VIS spectra of the luminescent compound [(Eu<sub>2</sub>Zr)(btc)<sub>3</sub>(Hbtc)<sub>0.5</sub>·6H<sub>2</sub>O)]; Figure S7: Exponential fitting of the decay curve of luminescent compound [(Eu<sub>2</sub>Zr)(btc)<sub>3</sub>(Hbtc)<sub>0.5</sub>·6H<sub>2</sub>O)].

**Author Contributions:** Conceptualization, A.R.B.S., M.d.O.J. and O.A.S.; Data curation, A.R.B.S., T.R.C., J.F.d.L., M.F.d.O. and S.A.J.; Formal analysis, A.R.B.S. and M.d.O.J.; Funding acquisition, O.A.S.; Investigation, M.d.O.J.; Methodology, A.R.B.S. and M.d.O.J.; Project administration, O.A.S.; Resources, O.A.S.; Supervision, O.A.S.; Writing—original draft, A.R.B.S. and M.d.O.J.; Writing—review and editing, A.R.B.S., J.F.d.L., M.F.d.O., S.A.J. and M.d.O.J. All authors have read and agreed to the published version of the manuscript.

**Funding:** The authors acknowledge the financial support from CNPq (426467/2018-3, O.A.S.), CAPES, FAPESP (2018/07514-3, O.A.S.) and FACEPE (BFP-0202-1.06/20 A.R.B.S.). M.d.O.J. is grateful for a CNPq grant (n° 311069/2020-7).

**Informed Consent Statement:** Not applicable.

**Data Availability Statement:** Solid state NMR data available at: de Oliveira Junior, Marcos. (2022). Solid state NMR data of amorphous MOF [(Eu<sub>2</sub>Zr)(btc)<sub>3</sub>(Hbtc)<sub>0.5</sub>·6H<sub>2</sub>O)] [Data set]. Zenodo. <https://doi.org/10.5281/zenodo.7311799>.

**Acknowledgments:** We would like to thank Cynthia Maria de Campos Prado Manso for fruitful discussions.

**Conflicts of Interest:** The authors declare no conflict of interest.

## References

1. Eliseeva, S.V.; Bünzli, J.-C.G. Rare earths: Jewels for functional materials of the future. *New J. Chem.* **2011**, *35*, 1165. [CrossRef]
2. Filho, P.C.S.; Larquet, E.; Drago, D.; Serra, O.A.; Gacoin, T. Lanthanoid-doped phosphate/vanadate mixed hollow particles as ratiometric luminescent sensors. *ACS Appl. Mater. Interfaces* **2017**, *9*, 1635. [CrossRef]
3. Nascimento, L.F.; Lima, J.F.; de Filho, P.C.; Serra, O.A. Control of diesel particulate emission based on Ag/CeO<sub>x</sub>/FeO<sub>y</sub> catalysts supported on cordierite. *Chem. Eng. J.* **2016**, *290*, 454. [CrossRef]
4. Huang, X.; Han, S.; Huang, W.; Liu, X. Enhancing solar cell efficiency: The search for luminescent materials as spectral converters. *Chem. Soc. Rev.* **2013**, *42*, 173. [CrossRef]
5. Nascimento, L.F.; Serra, O.A. Washcoating of cordierite honeycomb with ceria-copper mixed oxides for catalytic diesel soot combustion. *Process Saf. Environ. Prot.* **2016**, *101*, 134. [CrossRef]
6. Cotton, S. *Lanthanoid and Actinide Chemistry*; John Wiley & Sons, Ltd.: Chichester, UK, 2006.
7. Bünzli, J.-C.G.; Moret, E.; Foiret, V.; Schen, K.J.; Mingzhao, W.; Linpei, J. Structural and photophysical properties of europium(III) mixed complexes with  $\beta$ -diketonates and o-phenanthroline. *J. Alloys Compd.* **1994**, *208*, 107. [CrossRef]
8. Filho, E.V.; de Filho, P.C.; Serra, O.A.; Weber, I.T.; Lucena, M.A.M.; Luz, P.P. New luminescent lanthanoid-based coordination compounds: Synthesis, studies of optical properties and application as marker for gunshot residues. *J. Lumin.* **2018**, *202*, 89. [CrossRef]
9. Júnior, J.C.A.; Santos, G.L.; Colaço, M.V.; Barroso, R.C.; Ferreira, F.F.; Santos, M.V.; de Campos, N.R.; Marinho, M.V.; Jesus, L.T.; Freire, R.O.; et al. New Eu(III) pyromellitic Metal–Organic Framework of intense red-orange luminescence and high thermal stability for marking in gunshot residues. *J. Phys. Chem. C* **2020**, *124*, 9996. [CrossRef]
10. Talhari, A.L.R.; Lucena, M.A.M.; Mauricio, F.G.M.; Oliveira, M.F.L.; Veiga-Souza, F.H.; Alves, S., Jr.; Weber, I.T. Luminescent marker for GSR: Evaluation of the acute oral and inhalation toxicity of the MOF [Eu(DPA)(HDP)]. *ACS Appl. Bio Mater.* **2020**, *3*, 3049. [CrossRef]
11. Weber, I.T.; Melo, A.J.; Lucena, M.A.; Consoli, E.F.; Rodrigues, M.O.; de Sá, G.F.; Maldaner, A.O.; Talhavini, M.; Alves, S., Jr. Use of luminescent gunshot residues markers in forensic context. *Forensic Sci. Int.* **2014**, *244*, 276. [CrossRef]
12. Lima, P.P.; Nobre, S.S.; Freire, R.O.; Júnior, S.A.; Ferreira, R.A.S.; Pischel, U.; Malta, O.L.; Carlos, L.D. Energy transfer mechanisms in organic–inorganic hybrids incorporating europium(III): A quantitative assessment by light emission spectroscopy. *J. Phys. Chem. C* **2007**, *111*, 17627–17634. [CrossRef]
13. Liu, K.; Jia, G.; Zheng, Y.H.; Song, Y.H.; Yang, M.; Huang, Y.J.; Zhang, L.H.; You, H.P. Room-temperature synthesis and luminescence properties of Eu<sup>3+</sup>/Tb<sup>3+</sup>-doped La(1,3,5-btc)(H<sub>2</sub>O)<sub>6</sub>. *Inorg. Chem. Comm.* **2009**, *12*, 1246. [CrossRef]
14. de Roo, J.; Baquero, E.A.; Coppel, Y.; de Keukeleere, K.; van Driessche, I.; Nayral, C.; Hens, Z.; Delpéch, F. Insights into the Ligand Shell, Coordination Mode, and Reactivity of Carboxylic Acid Capped Metal Oxide Nanocrystals. *ChemPlusChem* **2016**, *81*, 1216. [CrossRef]

15. Ye, B.H.; Li, X.Y.; Williams, I.D.; Chen, X.M. Synthesis and structural characterization of di- and tetranuclear zinc complexes with phenolate and carboxylate bridges. Correlations between  $^{13}\text{C}$  NMR chemical shifts and carboxylate binding modes. *Inorg. Chem.* **2002**, *41*, 6426. [[CrossRef](#)] [[PubMed](#)]
16. Faccini, F.; Fric, H.; Schubert, U.; Wendel, E.; Tsetsgee, O.; Müller, K.; Bertagnolli, H.; Venzo, A.; Gross, S.  $\omega$ -Mercapto-functionalized hafnium- and zirconium-oxoclusters as nanosized building blocks for inorganic-organic hybrid materials: Synthesis, characterization and photothiol-ene polymerization. *J. Mater. Chem.* **2007**, *17*, 3297. [[CrossRef](#)]
17. Dutra, J.D.L.; Bispo, T.D.; Freire, R.O. LUMPAC lanthanoid luminescence software: Efficient and user friendly. *J. Comput. Chem.* **2014**, *35*, 772. [[CrossRef](#)]
18. Jaeger, C.; Hemmann, F. EASY: A simple tool for simultaneously removing background, deadtime and acoustic ringing in quantitative NMR spectroscopy—Part I: Basic principle and applications. *Solid State Nucl. Magn. Reson.* **2014**, *57*, 22. [[CrossRef](#)]
19. Cory, D.G.; Ritchey, W.M. Suppression of signals from the probe in Bloch decay spectra. *J. Magn. Reson.* **1988**, *80*, 128. [[CrossRef](#)]
20. Bennett, A.E.; Rienstra, C.M.; Auger, M.; Lakshmi, K.V.; Griffin, R.G. Heteronuclear decoupling in rotating solids. *J. Chem. Phys.* **1995**, *103*, 6951. [[CrossRef](#)]
21. Baccile, N.; Laurent, G.; Bonhomme, C.; Innocenzi, P.; Babonneau, F. Solid-state NMR characterization of the surfactant-silica interface in templated silicas: Acidic versus basic conditions. *Chem. Mater.* **2007**, *19*, 1343. [[CrossRef](#)]
22. Christiansen, S.C.; Hedin, N.; Epping, J.D.; Janicke, M.T.; del Amo, Y.; Demarest, M.; Brzezinski, M.; Chmelka, B.F. Sensitivity considerations in polarization transfer and filtering using dipole-dipole couplings: Implications for biomineral systems. *Solid State Nucl. Magn. Reson.* **2006**, *29*, 170. [[CrossRef](#)] [[PubMed](#)]
23. Wiench, J.W.; Bronnimann, C.E.; Lin, V.S.-Y.; Pruski, M. Chemical shift correlation NMR spectroscopy with indirect detection in fast rotating solids: Studies of organically functionalized mesoporous silicas. *J. Am. Chem. Soc.* **2007**, *129*, 12076. [[CrossRef](#)] [[PubMed](#)]
24. Mafra, L.; Siegel, R.; Fernandez, C.; Schneider, D.; Aussenac, F.; Rocha, J. High-resolution  $^1\text{H}$  homonuclear dipolar recoupling NMR spectra of biological solids at MAS rates up to 67 KHz. *J. Magn. Reson.* **2009**, *199*, 111–114. [[CrossRef](#)]
25. Kimura, H.; Nakamura, K.; Eguchi, A.; Sugisawa, H.; Deguchi, K.; Ebisawa, K.; Suzuki, E.I.; Shoji, A. Structural study of  $\alpha$ -amino-acid crystals by 1H CRAMPS NMR spectroscopy. *J. Mol. Struct.* **1998**, *447*, 247. [[CrossRef](#)]
26. Potrzebowski, M.J.; Tekely, P.; Dusausoy, Y. Comment to  $^{13}\text{C}$ -NMR studies of  $\alpha$  and  $\gamma$  polymorphs of glycine. *Solid State Nucl. Magn. Reson.* **1998**, *11*, 253. [[CrossRef](#)]
27. Nakamoto, K. *Infrared and Raman Spectra of Inorganic and Coordination Compounds*, 6th ed.; John Wiley & Sons, Inc.: New York, NY, USA, 2006.
28. Babij, N.R.; McCusker, E.O.; Whiteker, G.T.; Canturk, B.; Choy, N.; Creemer, L.C.; Amicis, C.V.D.; Hewlett, N.M.; Johnson, P.L.; Knobelsdorf, J.A.; et al. NMR chemical shifts of trace impurities: Industrially preferred solvents used in process and green chemistry. *Org. Process Res. Dev.* **2016**, *20*, 661. [[CrossRef](#)]
29. Cai, Z.; Wei, C.; Sun, B.; Wei, H.; Liu, Z.; Bian, Z.; Huang, C. Luminescent europium(III) complexes based on tridentate isoquinoline ligands with extremely high quantum yield. *Inorg. Chem. Front.* **2021**, *8*, 41. [[CrossRef](#)]
30. Barbosa, C.D.; Da Luz, L.L.; Paz, F.A.; Malta, O.L.; Rodrigues, M.; Júnior, S.A.; Ferreira, R.A.; Carlos, L.D. Site-selective Eu(III) spectroscopy of highly efficient luminescent mixed-metal Pb(II)/Eu(III) coordination polymers. *RSC Adv.* **2017**, *7*, 6093. [[CrossRef](#)]
31. Capobianco, J.A.; Proulx, P.P.; Bettinelli, M.; Negrisoló, F. Absorption and emission spectroscopy of  $\text{Eu}^{3+}$  in metaphosphate glasses. *Phys. Rev. B Condens. Matter.* **1990**, *42*, 5936. [[CrossRef](#)]
32. Nogami, M.; Umehara, N.; Hayakawa, T. Effect of hydroxyl bonds on persistent spectral hole burning in  $\text{Eu}^{3+}$ -doped  $\text{BaO-P}_2\text{O}_5$  glasses. *Phys. Rev. B* **1998**, *58*, 6166. [[CrossRef](#)]
33. de Oliveira, M., Jr.; Gonçalves, T.S.; Ferrari, C.; Magon, C.J.; Pizani, P.S.; de Camargo, A.S.S.; Eckert, H. Structure–Property Relations in Fluorophosphate Glasses: An Integrated Spectroscopic Strategy. *J. Phys. Chem. C* **2017**, *121*, 2968. [[CrossRef](#)]
34. Galaço, A.R.B.S.; Freire, R.O.; de Jesus, L.T.; Serra, O.A. Experimental and Theoretical study of isorecticular lanthanoid organic framework (LOF): Structure and luminescence. *J. Lumin.* **2020**, *223*, 179.